# Physicochemical-microstructural approach for modeling the crack passage at topside metallic parts in IGBT semiconductor power electronics

Mustafa Shqair, Zoubir Khatir, Ali Ibrahim, Mounira Bouarroudj-Berkani, Ayda Halouani, Tayssir Hamieh

# Physicochemical-microstructural approach for modeling the crack passage at topside metallic parts in IGBT semiconductor power electronics

M. Shqair*, Z. Khatir, A. Ibrahim, M. Berkani, A. Halouani, T. Hamieh
Gustave Eiffel University, 25 allée des marronniers, 78000 Versailles, France
mustafa.shqair@univ-eiffel.fr

**Abstract**

Insulated-gate bipolar transistors (IGBTs) are widely used components in power electronics applications. Upon operation, the difference in thermal expansion coefficients of materials composing the upper metallic parts causes thermal fatigue. The latter leads to degradations at metallic topside interconnections through the formation of cracks [1]. This paper focuses on a new physicochemical-microstructural approach for modeling the crack propagation at the contact interface between wires and metallization layers in a power module to answer the following question: what is the preferential crack path along the interface, and what are the influencing parameters? The model is based on a cohesive zone model (CZM) approach [2] in the vicinity of the contact, used for predicting the crack propagation pathway in a small interfacial region on either sides of a contact. In order to achieve such predictability, CZM parameters are linked to physicochemical-microstructural properties, i.e. the crack propagation is interpreted at the metallic contact zone based on this linkage. Therefore, the originality of this work lies on the combination of a fracture mechanics approach and a physicochemical-microstructural one.

## 1. General review

Several multi-physics finite elements models discussed the problem of fatigue of topside metallic compartments of power modules without taking into account the microstructural features. The microstructure of metallic compartments is composed of connected grains, which are the monomers of polycrystalline materials, separated by grain boundaries.

Some physicochemical studies were initially done for analyzing such problems in metals, however in the cases of steady state heating at high temperatures [3]. Such conditions are completely different from the degradations occurring in power modules, where the effect of the continuous temperatures fluctuations is not considered.

Lately, attempts were exerted to consider the effect of cycling. Martineau et al. [1] explained in details the mechanisms of the microstructural changes taking place upon the metallization's degradation. Loh et al. [4] found that the crack propagation is much slower for wires bonded at higher temperatures, which can be attributed to the coarser grain sizes resulting at the metallization-wire interface. Pederson et al. [5] related the crack propagation pathway with grains reconstructions, which are affected by the maximum subjected temperature and the junction temperature value. Sangid et al. [6] explained in details a dislocation based model for the crack initiation between neighboring grains. The effect of the grain size and the disorientation angle on the fatigue crack growth was seen by Zhou et al. [7]. When the grain size decreases, the rate of the crack propagation decreases as well, whereas when the disorientation angle increases, the rate of the crack propagation decreases. From all the preceding, it has been seen that there is a great dependence between fatigue and various physicochemical-microstructural features.

One of the most famous models which predicts the crack propagation process is the CZM. The latter is a finite element multi-physics model in fracture mechanics, in which the fracture formation is regarded as a gradual phenomenon through the separation of intersecting surfaces. The crack propagation is controlled by the values of the cohesion energy of the intersecting materials in addition to their strength.

Since the crack propagation process is the driving force for total failure, relationships were aimed to be constructed between the parameters of the CZM and main physicochemical-microstructural properties. This paper serves to model this dependency, through relating physiochemical-microstructural features to the crack propagation. The goal of this new and original model is to predict the crack passage at the wire-metallization interconnections from a physicochemical-microstructural point of view by the help of fracture mechanics approaches, and to confirm this approach experimentaly.

## 2. Relating the CZM parameter to physicochemical-microstructural factors

Based on previously done aging experiments on SKIM63 IGBT modules [8], further microstructural analysis were carried on. Using such data, and starting from the linkage between the crack propagation process and various physicochemical-microstructural features, some relationships are considered.

### i. Fracture energy

The first CZM parameter to consider is the fracture energy. The work of separation of intersecting surfaces ($W_{sep}$) is used for representing such parameter [9], where grain boundaries are considered as intersecting surfaces. This parameter is linked to both surface energy and grain boundary energy ($\gamma_s$ and $\gamma_{gb}$) as shown in equation (1).

$$W_{sep} = \gamma_{s1} + \gamma_{s2} - \gamma_{gb} \quad (1)$$

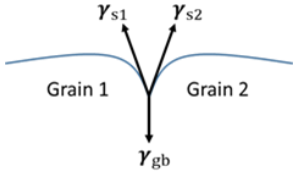


*Figure 1: A schematization of two neighbor grains.*

From preceding, the values of $\gamma_s$ and $\gamma_{gb}$ are necessary for obtaining $W_{sep}$. The values of $\gamma_s$ depend on the grains texture. At temperatures highly lower than the melting point of the material (as in power cycling), the effect of reached temperatures on $\gamma_s$ values is minimal [10]. From EBSD data the planes of orientation of grains can be deduced referring to reference [11]. For aluminum, the surface energy values for the following orientations (100), (101) and (111) have surface energy values of 0.9 J/m$^2$, 0.972 J/m$^2$ and 0.62 J/m$^2$ respectively.

For simplification, for a non-degraded IGBT sample as shown in Figure 2, only the heel interconnection positions are considered. Heel positions are the places of cracks initiation [12]. It is observed that different grain orientations exist as seen in Figure 3, thus the values of surface energies vary.

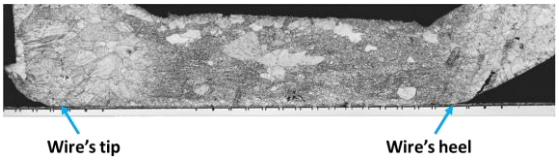


*Figure 2 : Healthy metallic interconnection of a SKIM63.*

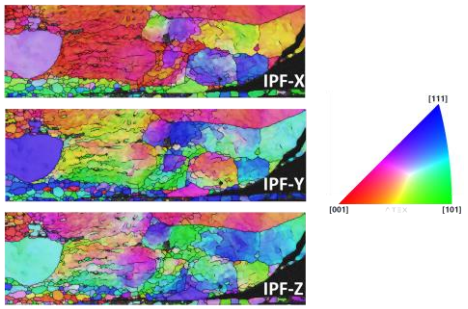


*Figure 3 : IPFs showing the planes of orientations of grains at the heel position in directions X, Y and Z.*

The value of $\gamma_{gb}$ depends on the disorientation angle between grains and the orientation angle of each single grain as represented in equation (2) [7].

$$0° < \Delta\theta < \theta_1 \text{ then } \gamma_{gb} = k\,\Delta\theta / \theta_1 \quad (2a)$$

$$\theta_1 < \Delta\theta < \theta_2 \text{ then } \gamma_{gb} = k \quad (2b)$$

$$\theta_2 < \Delta\theta < 90° \text{ then } \gamma_{gb} = [k\,(90 - \Delta\theta) / (90 - \theta_2)] \quad (2c)$$

Where $\Delta\theta$ is the disorientation angle between grains, k is the Hall-Petch constant and $\theta_i$ is the orientation angle of each individual grain (i).

Using the ATEX program, the values of orientation and disorientation angles can be extracted. The existence of various grain orientation and disorientation angles can be well seen in Figure 4 and Figure 5 successively.

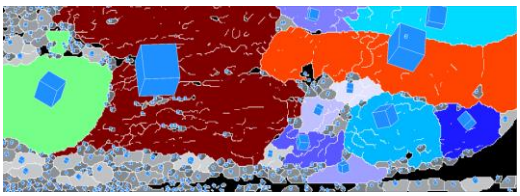

*Figure 4 : Grains crystal orientations reflecting the presence of different orientation angles.*

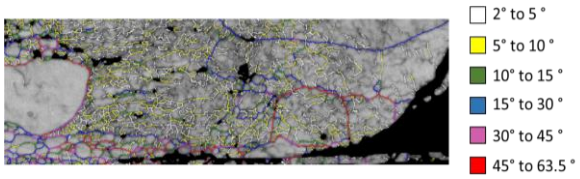


*Figure 5 : Grains disorientation angles distribution.*

From Figure 4, it can be deduced that grains have different crystal orientations, thus high variation in the values of grains orientation angles. Figure 5 shows that low angle boundaries are present above the wire-metallization interconnection whereas high angle boundaries exist just at the metallic interface. Referring to equations (1) and (2), grains above the interconnection have lower boundary energies and higher cohesive energies than those just at the metallic interconnection.

After knowing the necessary parameters for calculating both surface and boundary energies, the work of separation parameter representing the fracture energy is obtained using equation (1).

**ii. Critical fracture stress**

The second CZM parameter to obtain is the critical stress. Since this parameter has a pure mechanical concept, the closest parameter to it when considering the normal direction is the tensile strength as mentioned in the ANSYS verification manual [13]. Tensile strength ($\sigma_{TS}$) is a more flexible parameter to use, where physicochemical-microstructural properties can be related to it. Yield strength, which is directly related to the tensile strength, is highly dependent on the grain size, since both parameters are inversely proportional according to the Hall-Petch equation [14].

$$\sigma_y = \sigma_0 + k\,d^{-0.5} \quad (3)$$

Where $\sigma_y$ is the yield stress, $\sigma_0$ is the friction stress, k is the Hall-Petch constant and d is the grain size.

Yield and tensile strengths are also related to the hardness value (H) as represented in equations (4) and (5), where (n) is the strain hardening exponent.

$$\sigma_y = (0.1)^n\,(H/3) \quad (4)$$

$$\sigma_{TS} = (n/0.217)^n\,(H/2.9) \quad (5)$$

Hardness values were obtained by doing some nanoindentation tests, however it was not possible to do them exactly at the metallic interconnection edges since the thickness of the wire there is small, especially after the wire welding process. Due to this limitation, in addition to the limitation of not knowing accurately the strain hardening exponent for each grain (0.05-0.2 [15]), additional method was used for obtaining the value of the tensile strength.

The strength of the bonded wire is highly lower than that of the metallization [16], and since experimentally cracks are not propagating inside the metallization, the precision in assuming the strength value for the grains of the metallization layer is not highly essential. Wire zones just above the metallization are the positions for the cracks passage, therefore the main focus is there.

Grains inside the metallization layer have almost the same small size, with an average tensile strength of about 175 MPa by looking at the average ratio of the tensile strength to the yield strength for different aluminum thin films thickness in reference [17] in addition to looking at the average hardness values then using equation (5).

Grains inside the wire are different especially in terms of size, therefore the tensile strength values are highly local. From reference [18] a relationship was established between the tensile strength and hardness. This relationship was applied on MOSFETs aluminum wires, by the help of nanoindentation tests necessary for obtaining the hardness values. When comparing the hardness values obtained in this article at the metallic interconnection sites with our values, big compatibility was observed, where the values are ranging between 450-550 MPa. The corresponding tensile stress values for such hardness values vary between 80-120 MPa. This range is due to the local characteristics of grains such as the grain size, where smaller grains acquire higher strength. These values are used in our model as tensile stress values inside the wire at the interconnection zone.

## 3. Modeling the crack passage using ANSYS APDL

Using the previous relationships, the CZM parameters can be deduced based on some experimental analysis. The prediction of the crack propagation process can be then achieved by using the ANSYS software.

For simplification, 2D electro-thermo-mechanical simulations were applied on a single SKIM63 IGBT chip, with the geometrical dimensions and materials properties listed in Table 1 and Table 2 [19]. Non-linear mechanical properties of copper and aluminum for both the metallization and the wire are presented in Figure 6 [20], [21].

A weak thermo-mechanical coupling was chosen in the simulations due to the minor effect that the mechanical behavior has on the thermal results. Thus, two consecutive electro-thermal and mechanical simulations were applied to represent the power cycling process. The first one was applied for the whole system to obtain the thermal gradients distribution. Then, the resulting thermal data are used as loads for the mechanical simulation which is associated with the mixed-mode CZMs. Since the computation time is high, only few cycles can be reasonably simulated in order to see the initial propagation path of the crack.

*Table 1 : The dimensions of SKIM63 modules.*

| Material | Length (mm) | Width (µm) |
|---|---|---|
| **Aluminum wire (Al)** | 13.9 | 380 |
| **Metallization layer (Al)** | 6.2 | 5 |
| **Silicon (Si)** | 7.7 | 140 |
| **Silver (Ag)** | 7.7 | 20 |
| **Superior Copper (Cu)** | 36 | 300 |
| **Ceramic (Al2O3)** | 39 | 380 |
| **Inferior Copper (Cu)** | 36 | 300 |
| **Superior thermal interface (TIM)** | 38 | 100 |
| **Aluminum plate (Al)** | 170 | 5000 |
| **Inferior thermal interface (TIM)** | 170 | 100 |
| **The cooling system (Al)** | 170 | 10000 |

*Table 2 : Material properties of SKIM63 components.*

| | Al | Si | Ag | Cu | $Al_2O_3$ | TIM |
|---|---|---|---|---|---|---|
| Density ($Kg/m^3$) | 2700 | 2330 | 7350 | 8960 | 3780 | - |
| Electric resistivity (Ω.m) | 2.7e-8 | $R_x$ >>> $R_y$ | 4e-8 | 1.7e-8 | 1e12 | 1e20 |
| Thermal conductivity (W/m.K) | 238 | 124 | 250 | 390 | 24 | 2 |
| Thermal capacity (J/Kg.K) | 897 | 750 | 230 | 390 | 830 | - |
| Poisson ratio | 0.33 | 0.3 | 0.37 | 0.34 | 0.2 | 0.33 |
| CET (ppm/K) | 23.5 | 4.1 | 19.6 | 17 | 8 | 23.5 |
| Young modulus (GPa) | 76 | 131 | 6.28 | 97 | 370 | 76 |

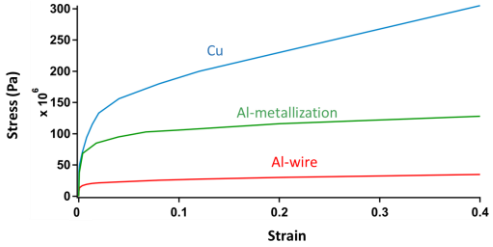


*Figure 6 : Elastoplastic stress–strain behaviors for aluminum and copper.*

Grains at the heel metallic interconnection interface were represented by hexagonal geometries, where CZM elements were applied on their boundaries. Hexagons are somehow close to the shape of grains which do not have really specific shapes when looking at the EBSD images as in Figure 3. Such geometry offers some curvature at the edges center as in real grains, in addition, it is flexible to control, by which the CZM elements can be assigned to its edges. In this model each hexagon has a radius of 3.54 µm close to the radius of grains.

The variation of grain sizes and angles of orientations between neighbouring grains were taken into account by using localized CZM parameters in accordance with the local microstructural characteristics observed in IGBT structures. Experimentally, it was observed that three different size zones exist at the heel position as seen in Figure 7. For this reason, these size zones were assumed to exist at the heel metallic interconnection interface as represented in Figure 8, so that localized CZM elements can be assigned separately for each zone.

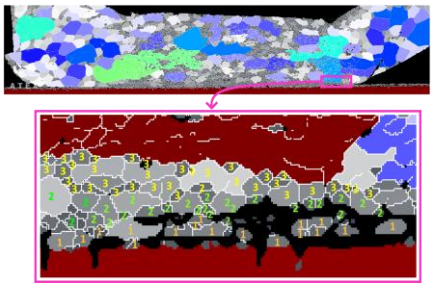

*Figure 7 : Grains numbered 1, 2 and 3 representing the size zones 1, 2 and 3.*

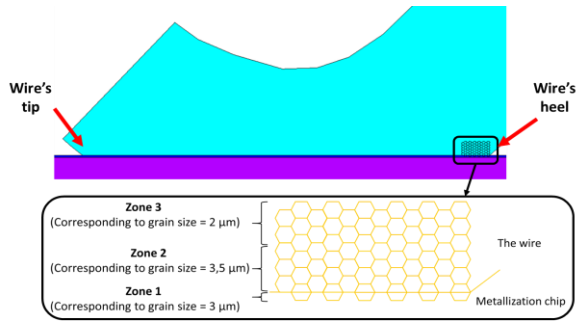


*Figure 8 : The three hexagon sizes zones inserted at the heel position corresponding to the zones seen in Figure 7.*

Since grains representing the zone 3 have a dominance in low angle boundaries and those representing the zone 2 have a dominance in high angle boundaries, then the hexagons in zone 3 are assumed to have higher critical energy values than those in zone 2 according to equation (1). Concerning the critical stress values, hexagons in zone 1 have higher values than those for zones 2 & 3 since thin films have higher strength than thick wires, in addition to the presence of 1% Si inside the metallization.

To model the crack formation, mixed mode CZMs were applied. Such models consist of normal and tangential fracture energies and critical stresses, in addition to a damping coefficient of 10 µs. The same values of stress in both normal and tangential directions were put because the ratio between both directions is not clear, in this way the same probability of cracking is offered for both directions. Therefore, tensile stress values representing the critical normal stress for crack formation as mentioned previously are used also for the tangential direction. As for the stresses, the values of energies were also put the same for both directions.

Because the critical stress values are high compared to the generated stresses at early cycling, these values were reduced. The aim of this reduction is speeding up the crack formation process to see it in few cycles. The reducing factor was assumed to be 3.2 for the hexagons inside the wire. This value if used for the hexagons of the metallization layer, cracks dominant there and this is illogical since metallization layers have clearly higher real tensile strength values than that for the wires, in addition, this cracking manner is not observed experimentally. Thus a smaller factor of a value of 2.25 is used. Then, for all the hexagons edges in zones 1, 2 and 3, the normal and tangential critical stresses are 78 MPa (175/2.25), 25 MPa (80/3.2) and 34.4 MPa (110/3.2) respectively, and the normal and tangential critical energies are 1 J/m$^2$, 1 J/m$^2$ and 1.8 J/m$^2$ respectively.

Five electro-thermal simulation cycles were made by inserting a current density of 7337 Amps/m$^2$ (≈ 56.5 Amps) at the upper metallic part for 3 s ($t_{on}$), this induced a voltage ≈ 2 volts. The sample is then relaxed for 6 s ($t_{off}$). Convection of 1500 W/m$^2$.K was applied at the lower part of the module to cool the module at the $t_{off}$ with an ambient temperature of 45°C. The resulting junction temperature from cycling is ΔT=110°C. This ΔT value is specifically chosen since it corresponds to previously done experimental tests [8]. The resulting temperature fluctuations at the upper metallic interconnection surface can be seen in Figure 9.

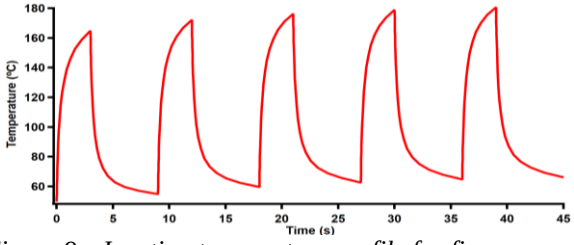


*Figure 9 : Junction temperature profile for five power cycles.*

The thermal results of this simulation were then used in the mechanical simulation. Only the upper metallic parts are considered in this simulation because major deformations occur there. In this simulation constraints with zero deformations were applied at the bottom edges of the superior layer of copper, where one vertex was constrained in both x and y directions whereas the second vertex was only constrained on the y direction. In this simulation the CZMs are activated. The resulting Normal stresses ($\sigma_x$ and $\sigma_y$) and shear stresses ($\sigma_{xy}$) values at the heel position are plotted for the three hexagon size zones at the end of the five cycles in Figure 10, Figure 11 and Figure 12 (unit is MPa). Stress values let us predict debonding (cracks formation) depending on the critical stresses values whether they are exceeded or not. Stress values decrease when debonding occurs, reaching null when debonding is complete.

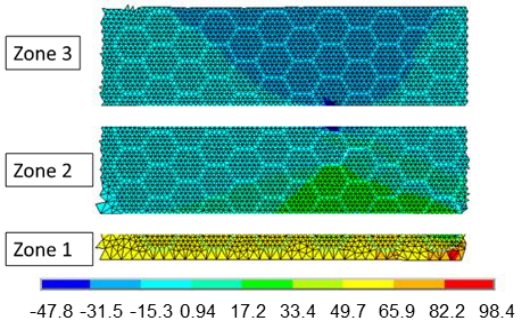


*Figure 10 : $\sigma_x$ values at the heel position after 5 cycles.*

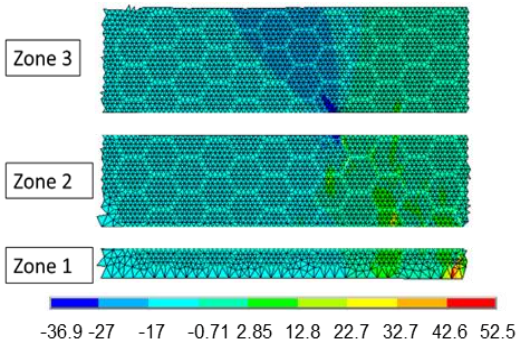


*Figure 11 : $\sigma_{xy}$ values at the heel position after 5 cycles.*

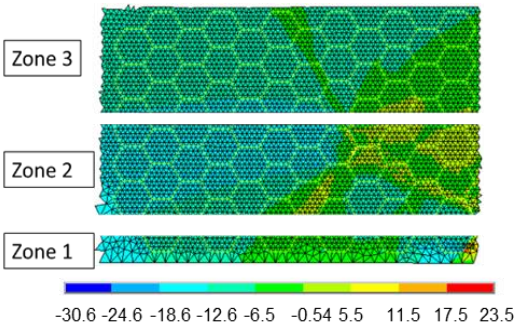


*Figure 12 : $\sigma_y$ values at the heel position after 5 cycles.*

From these figures, debonding preferably occurs in zone 2. This is deduced from the presence of certain stress values exceeding the critical stresses. For verifying that, the debonding map is plotted at the heel zone in Figure 13. The debonding factor is 0 in the initial state before cycling. When debonding begins, the value increases until reaching a value of 1 signifying the occurrence of total debonding.

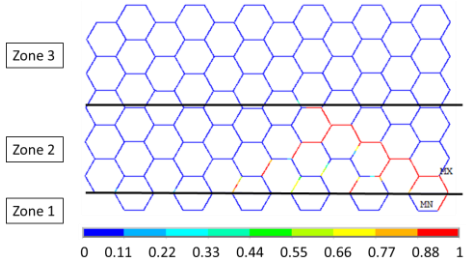


*Figure 13 : The debonding map at the heel after 5 cycles.*

The same simulations were then applied at the tip metallic interconnection. Cracks formation speed was observed to be slower than that at the heel position after plotting the debonding map as seen in Figure 14. This probably signifies that cracks start formation primarily at the heel position and then after several number of cycles cracks start to form at the tip.

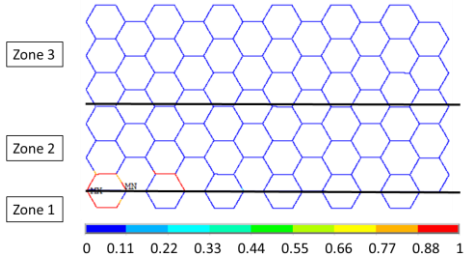


*Figure 14 : The debonding map at the tip after 5 cycles.*

Starting from the previously presented relationships, different conclusions can be presented from the simulations. First, debonding occurs inside the wire just above the metallic interconnection interface. Debonding did not take place inside the metallization due to the high strength it acquires as detailed previously. In addition, debonding seems to start from terminal hexagons at both heel and tip metallic interconnections. The reason behind that is the existence of maximal stresses at those positions. Debonding speed was observed to be higher at the heel than at the tip interconnection.

The simulations results were then compared to SEM images in order to validate the relevance between both experimental and numerical crack propagation manners. Figure 15 signifies that heel interconnection positions are the first sites of cracks formation with higher speed than that at the tip. Cracks continue growing from the extremities until reaching the center. At this moment the crack becomes totally distributed at the bottom wire zone, where lifting off occurs.

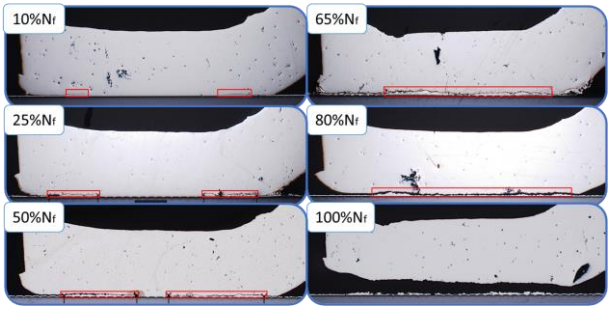


*Figure 15 : The crack propagation manner upon cycling.*

Some factors affecting on the degradation process that numerical simulations cannot cover are listed as following. Cracks do not penetrate the wire bulk upon cycling, even though bigger grains are present, which are weaker grains according to the Hall-Petch relation. This is mainly because the wire welding process leads to the formation of high amount of plastic deformations at the metallic interconnection interface, enhancing the formation of cracks in such zones [22]. Additionally, from the wire welding process some impurities may result at the metallic interface, this weakens the grains there [23]. The presence of higher amount of low angle boundaries above the interconnection zone increases the fracture energy, thus cracks are harder to form inside the bulk. Grain boundaries may also act as geometrical hindrances for cracks due to the high difference in terms of grain sizes between grains at the metallic interconnection and inside the bulk [7], [24]. Grain reconstructions resulting at the interconnection interface is also an important cause for decreasing the contact between grains [25].

## 4. Conclusions

A new approach of modeling the crack formation and propagation processes at the metallic interconnection interfaces in semiconductor power modules was presented in this paper. This approach was based on relating the parameters of a finite element Multiphysics model which is the CZM with physicochemical-microstructural properties. Such combination enables us to predict the crack formation and propagation. For this aim, some simulations were then carried on using the ANSYS software by applying 2D electro-thermo-mechanical simulations, benefiting from the relationships shown previously. Cracks resulting in such simulations were in accordance with the experimental results obtained from the SEM analysis. Cracks initiate at the terminal edges of the wire-metallization interconnection at the heel position with higher speed than that at the tip. Such study has the

advantage of enabling us to understand the manner of cracks formation, and the main parameters affecting on it, through interpreting sensible and observable issues, which are the microstructural features.

**References**


[1] D. Martineau, C. Levade, M. Legros, P. Dupuy, and T. Mazeaud, "Microelectronics Reliability Universal mechanisms of Al metallization ageing in power MOSFET devices," *Microelectron. Reliab.*, vol. 54, pp. 2432–2439, 2014.

[2] K. Park and G. H. Paulino, "Cohesive zone models: A critical review of traction-separation relationships across fracture surfaces," *Appl. Mech. Rev.*, vol. 64, p. 20, 2011.

[3] W. W. Mullins, "Theory of linear facet growth during thermal etching," *Philos. Mag.*, vol. 6, pp. 1313–1341, 1961.

[4] W. Loh, M. Corfield, H. Lu, S. Hogg, T. Tilford, and C. M. Johnson, "Wire Bond Reliability for Power Electronic Modules - Effect of Bonding Temperature," in *Thermal, Mechanical and Multi-Physics Simulation Experiments in Microelectronics and Micro-Systems*, 2007, p. 6.

[5] K. B. Pedersen, L. H. Østergaard, P. K. Kristensen, P. Ghimire, V. N. Popok, and K. Pedersen, "Degradation evolution in high power IGBT modules subjected to sinusoidal current load," *J. Mater. Sci. Mater. Electron.*, vol. 27, pp. 1938–1945, 2016.

[6] M. D. Sangid, H. J. Maier, and H. Sehitoglu, "The role of grain boundaries on fatigue crack initiation - An energy approach," *Int. J. Plast.*, vol. 27, pp. 801–821, 2011.

[7] P. Zhou, J. Zhou, Z. Ye, X. Hong, H. Huang, and W. Xu, "Effect of grain size and misorientation angle on fatigue crack growth of nanocrystalline materials," *Mater. Sci. Eng. A*, vol. 663, pp. 1–7, 2016.

[8] N. Dornic, "Élaboration et comparaison de deux modèles de durée de vie des fils d'interconnexion des modules de puissance, l'un basé sur les déformations et l'autre sur les dégradations," 2020.

[9] J. J. Möller and E. Bitzek, "Fracture toughness and bond trapping of grain boundary cracks," *Acta Mater.*, vol. 73, pp. 1–11, 2014.

[10] Z. Wang *et al.*, "Effects of finite temperature on the surface energy in Al alloys from first-principles calculations," *Appl. Surf. Sci.*, vol. 479, pp. 499–505, 2019.

[11] J. M. Zhang, F. Ma, and K. W. Xu, "Calculation of the surface energy of FCC metals with modified embedded-atom method," *Appl. Surf. Sci.*, vol. 229, pp. 34–42, 2004.

[12] D. O. Harris *et al.*, "Fracture Mechanics Life Prediction For Microscale Components – With Application to Wire Bonding," in *29th Annual Proceedings Reliability Physics*, 1991, pp. 35–43.

[13] ANSYS® Mechanical APDL 15.0, *ANSYS Mechanical APDL Verification Manual*. 2013.

[14] R. W. Armstrong, "The cleavage strength of pre-cracked polycrystals," *Eng. Fract. Mech.*, vol. 28, pp. 529–538, 1987.

[15] S. Kalpakjian and S. Schmid, "Mechanical Behavior, Testing, and Manufacturing Properties of Materials," in *Manufacturing Engineering & Technology*, 2010, pp. 56–87.

[16] M. Held, P. Jacob, G. Nicoletti, P. Scacco, and M. H. Poech, "Fast power cycling test for insulated gate bipolar transistor modules in traction application," *Int. J. Electron.*, vol. 86, pp. 1193–1204, 1999.

[17] H. Kubo, M. Ciappa, T. Masunaga, and W. Fichtner, "Multiscale simulation of aluminum thin films for the design of highly-reliable MEMS devices," *Microelectron. Reliab.*, vol. 49, pp. 1278–1282, 2009.

[18] M. S. Broll *et al.*, "Correlation between mechanical properties and microstructure of different aluminum wire qualities after ultrasonic bonding," *Microelectron. Reliab.*, vol. 55, pp. 1855–1860, 2015.

[19] SEMIKRON, *SKiM306GD12E4*. 2017, pp. 1–6.

[20] J. F. Shackelford and W. Alexander, *Materials Science & Engineering*. 2012.

[21] Y. Nagatomo, T. Nagase, and S. Shimamura, "FEM analysis of thermal cycle properties of the substrates for power modules," *J. Japan Inst. Electron. Packag.*, vol. 3, pp. 330–334, 2000.

[22] S. Buhrkal-Donau, "Comparative study of wire bond degradation under power and mechanical accelerated tests," 2018.

[23] J. Goehre, M. Schneider-Ramelow, U. Geißler, and K. D. Lang, "Interface degradation of Al heavy wire bonds on power semiconductors during active power cycling measured by the shear test," *2010 6th Int. Conf. Integr. Power Electron. Syst. CIPS 2010*, pp. 16–18, 2011.

[24] K. Dharmesh, I. Sridhar, W. Wei, and S. Narasimalu, "Effect of Surface Mechanical Treatments on the Microstructure-Property-Performance of Engineering Alloys," *Materials (Basel).*, vol. 12, p. 41, 2019.

[25] J. Zhao *et al.*, "A study on the effect of microstructure evolution of the aluminum metallization layer on its electrical performance during power cycling," *IEEE Trans. Power Electron.*, vol. 34, pp. 11036–11045, 2019.